

## Supporting Information

### Enhanced interface regulation via $\pi$ -conjugated heterojunctions for high-efficiency inverted perovskite solar cells

Qin Gao<sup>1</sup>, Can Wang<sup>1</sup>, Nabonswende Aida Nadege Ouedraogo<sup>1,\*</sup>, Ke Zhao<sup>2</sup>, Dingqin Hu<sup>3</sup>, Kun Chen<sup>4</sup>, Yi Pan<sup>1</sup>, Zeping Ou<sup>1</sup>, Mingyang Gao<sup>1</sup>, Lei Liu<sup>1</sup>, Junjie Zhang<sup>1</sup>, Teng Gu<sup>5</sup>, Gengsui Tian<sup>5</sup>, Pengyan Zhang<sup>5</sup>, Zeyun Xiao<sup>5</sup>, Haoxuan Guo<sup>6</sup>, Rui Wang<sup>2</sup>, Yujie Zheng<sup>1</sup>, Kuan Sun<sup>1,\*</sup>

<sup>1</sup>MOE Key Laboratory of Low-grade Energy Utilization Technologies and Systems, School of Energy & Power Engineering, Chongqing University, Chongqing 400044, China

<sup>2</sup>School of Engineering, Westlake University and Institute of Advanced Technology, Westlake Institute for Advanced Study, Hangzhou 310030, China

<sup>3</sup>Department of Mechanical Engineering, City University of Hong Kong, Kowloon Tong, Hong Kong 999077, China

<sup>4</sup>Research and Development Center, JA Solar, Yangzhou, 225131, China

<sup>5</sup>Chongqing Institute of Green and Intelligent Technology, Chinese Academy of Sciences, Chongqing 400714, China

<sup>6</sup>Department of Chemistry and Materials Engineering, Kansai University, Suita, Osaka, 564-8680, Japan

Correspondence: aida@cqu.edu.cn; kuan.sun@cqu.edu.cn

## Experimental Section

### Materials

Nickel oxide ( $\text{NiO}_x$ ) (particle size of 5-10 nm),  $\text{C}_{60}$  and formamidine hydroiodide (FAI) were purchased from Advanced Election Technology Co., Ltd. Methylammonium iodide (MAI), 1,2-propyldiammonium Diiodide ( $\text{PDAI}_2$ ) and bathocuproine (BCP) were purchased from Xi'an Yuri Solar Co., Ltd. [4-(3,6-dimethyl-9H-carbazol-9-yl) butyl] phosphonic Acid (Me-4PACz), methylammonium chloride (MACl), 1-benzyl-3-methylimidazolium tetrafluoroborate ( $\text{BzMIMBF}_4$ ) and lead iodide ( $\text{PbI}_2$ ) were purchased from TCI. Isopropanol (IPA), N, N-dimethylformamide (DMF), dimethyl sulfoxide (DMSO) and ethyl acetate (EA) were purchased from Sigma-Aldrich. All materials above are directly used without further purification.

### Device fabrication

Indium tin oxide (ITO) glass substrates were sequentially ultrasonicated in detergent, deionized water, acetone, and isopropanol for 15 minutes each, then dried with a nitrogen stream and subjected to UV-ozone treatment for 30 minutes to prepare for subsequent processing. A 10 mg/mL  $\text{NiO}_x$  nanoparticle dispersion in deionized water was stirred for 20 minutes, filtered, and spin-coated onto the substrates at 5000 rpm for 30 seconds, followed by annealing at 150 °C for 10 minutes in ambient air. The substrates were then transferred to a nitrogen-filled glovebox, where a 0.5 mg/mL Me-4PACz solution in isopropanol was spin-coated onto the  $\text{NiO}_x$  layer at 3000 rpm for 30 seconds and annealed at 100 °C for 10 minutes. For  $\text{BzMIMBF}_4$ -treated samples, solutions of  $\text{BzMIMBF}_4$  (0, 0.3, 0.5, and 1 mg/mL in a 1:9 DMF/isopropanol mixture) were spin-coated onto the Me-4PACz layer at 5000 rpm for 30 seconds, followed by annealing at 100 °C for 10 minutes. The perovskite precursor solution, composed of 1.7 M  $\text{FA}_{0.85}\text{MA}_{0.1}\text{Cs}_{0.05}\text{PbI}_3$  with 10 mol% MAcl and 5 mol% excess  $\text{PbI}_2$  to improve crystallinity and phase stability, was prepared using a one-step method. For deposition, 65  $\mu\text{L}$  of the precursor was spin-coated onto the substrate using a two-step program: 1000 rpm for 10 seconds,

then 5000 rpm for 40 seconds, with 200  $\mu\text{L}$  of ethyl acetate anti-solvent dripped 15 seconds before the end to promote nucleation. The resulting film was annealed at 100  $^{\circ}\text{C}$  for 30 minutes. A passivation solution of 1 mg/mL  $\text{PDAI}_2$  in isopropanol was prepared, and 80  $\mu\text{L}$  was dynamically spin-coated at 4500 rpm for 25 seconds (dispensed immediately upon reaching 4500 rpm), followed by annealing at 100  $^{\circ}\text{C}$  for 5 minutes. Finally, 24 nm  $\text{C}_{60}$ , 4 nm BCP, and 100 nm Ag layers were sequentially deposited via thermal evaporation. Furthermore, a layer of anti-reflective coating was applied to the illumination side of each device through spin-coating. The anti-reflection solution was obtained from 00 FIVE (CHONGQING) Nano Technology Co., Ltd.

### **Devices characterizations**

$^1\text{H}$  NMR spectra were obtained on a Bruker AVANCE III 600 MHz nuclear magnetic resonance (NMR) spectrometer. Photocurrent density-voltage ( $J$ - $V$ ) curves were measured using a solar simulator equipped with 450 W Xenon lamp (Newport 6279 NS) and a Keithley 2400 source meter. The effective active area of the device was defined to be 0.08  $\text{cm}^2$  (calibrated mask).  $J$ - $V$  curves were measured from -0.1 V to 1.2 V (forward scan, FS) or from 1.2 V to -0.1 V (reverse scan, RS) with a scan rate of 100 mV/s. Light intensity was adjusted to AM 1.5G one sun ( $100 \text{ mW cm}^{-2}$ ) with a NIM calibrated standard Si solar cell. The external quantum efficiency (EQE) measurement was conducted on an EQE measurement system. The scanning electron microscopy (SEM) images was acquired using a scanning electron microscopy (Thermo Scientific Quattro ESEM), which uses an electron beam accelerated at 200 V to 30 kV, enabling operation at a variety of currents. X-ray diffraction (XRD) patterns were acquired using a PANalytical Empyrean diffractometer equipped with Cu  $\text{K}\alpha$  radiation ( $\lambda = 1.5406 \text{ \AA}$ ). The surface morphology was characterized by atomic force microscope (AFM) (MicroNano NexSPM, Zhuolun). Absorption spectra were measured using a Shimadzu UV-1800 UV-vis spectrophotometer. The conductive Atomic Force Microscopy (c-AFM) mode was utilized with a Bruker Atomic Force Microscope (Model: Bruker

Dimension Icon) for testing. The SCM-PIT-V2 probe, featuring a force constant of 2.8 N/m and a resonance frequency of 75 kHz, was employed. The scanning image resolution was configured at 256×256 pixels with a scanning frequency of 0.5 Hz, ensuring high-precision imaging and dependable electrical data collection. XPS measurements were performed on a Thermo-Fisher ESCALab 250Xi system with a monochromatized Al K $\alpha$  (for XPS mode) under the pressure of  $5.0 \times 10^{-7}$  Pa. A Fluorescence spectrophotometer (Cary Eclipse, Agilent) with an excitation wavelength of 450 nm was used to collect steady state photoluminescence (PL) spectra. The photoluminescence (PL) and photocurrent mappings are performed on a home-built laser-scanned and time-resolved PL microscopy coupled with a photocurrent detection module. For PL measurements, a pulse laser (410 nm with 40 MHz repetition rate LDH-P-C-410, PicoQuant, Germany) is focused on the sample through a 60 X oil objective lens (NA = 1.4, Olympus UPlanSApo). The laser intensity at samples is adjusted by a neutral density filter and measured with a power meter (PM100D S130VC, Thorlabs, USA). The Atomic Force Microscope (AFM) and Kelvin Probe Force Microscopy (KPFM) measurements were conducted using an MFP-3D-BIO system from Oxford Instruments. The femtosecond transient absorption spectroscopy (fs-TAS) system utilized a high-performance 1046 nm ytterbium (Yb)-doped fiber laser oscillator, delivering 500  $\mu$ J ultrashort pulses at 2 kHz with an average power of  $\sim 1$  W and a temporal resolution of 283.9 fs (FWHM, confirmed by testing). It employs a sapphire-based white-light continuum for broadband probing across 480-950 nm, with optional modules extending coverage to ultraviolet (350-650 nm), near-infrared (1100-1600 nm), and short-wave infrared (1600-2400 nm) ranges, enabling comprehensive ultrafast photophysical studies from visible to mid-infrared wavelengths. Electrochemical workstation (Princeton VersaSTAT 3F) equipment was used. Grazing-incidence X-ray diffraction (GIXRD) measurements were conducted using Bruker D8Discover 25 X-ray diffractometer with power of 1.6 kW. Scanning speed is 2 second per step, 0.01 degree per step, with  $\psi$  angle from 10 to 50 degree. The incident X-ray beam was set to a fixed grazing angle of  $1^\circ$ , ensuring surface-sensitive analysis. Time-of-

flight secondary ion mass spectrometry (IONTOF GmbH, M6) was utilized to analyze ion migration characteristics. Ultraviolet photoelectron spectroscopy (UPS) of the thin films was performed using a Shimadzu Kratos spectrometer with a step size of 0.025 eV and a scan rate of 300, equipped with a non-monochromatic He I $\alpha$  photon source ( $h\nu = 21.22$  eV). The TPV measurement was performed under 1 sun illumination using a white LED, with the device configured to open-circuit conditions. The TPC measurement was conducted in the dark under short-circuit conditions. A Keysight oscilloscope was used to capture the output signal. The photovoltage decay kinetics for all devices exhibited a mono-exponential decay pattern. Transient photocurrent (TPC) tests were carried out under short-circuit conditions to investigate the time-dependent extraction of photo-generated charge carriers. A 10 ns laser pulse served as the light source. Devices were maintained in the dark between pulses to eliminate the impact of pulse frequency on current responses. Transient photovoltage (TPV) tests were conducted under open-circuit conditions to examine photovoltage decay. The subsequent voltage decay was recorded to directly assess non-geminate charge carrier recombination. The decay kinetics followed a mono-exponential model:  $\delta V = A \exp(-t/\tau)$ , where  $t$  represents time and  $\tau$  denotes the charge carrier lifetime.

## Density functional theory

The quantum chemistry calculations (monomer and simple cluster structures) were carried out with the Gaussian 16<sup>1</sup> software. The B3LYP<sup>2</sup> functional was adopted for all calculations in combination with the DFT-D3(BJ)<sup>3, 4</sup> dispersion correction. The basis set of def2-SVP<sup>5</sup> were adopted for the geometry optimization and frequency calculations. The geometries were fully optimized without any structural constraints. The frequency calculations were carried out at the same level of theory to verify that all structures have no imaginary frequency. The single energy was calculated at the def2-TZVP<sup>6</sup> level of theory. The Interaction Region Indicator (IRI)<sup>7</sup> and the electrostatic potential involved in the analyses was evaluated by Multiwfn<sup>8-10</sup> based on the highly effective algorithm proposed in Ref. The IRI and ESP figures were rendered by means of the VMD<sup>11</sup> visualization program.

The first principle calculations (periodicity structures) were carried out with the CP2K 2024.1 software package<sup>12</sup> with Perdew-Burke-Ernzerhof (PBE) functional<sup>11</sup> and Grimme's D3 van der Waals correction method<sup>3, 4</sup>, during which the DZVP-MOLOPT-SR-GTH<sup>13</sup> basis set and Goedecker-Teter-Hutter (GTH) pseudopotential were employed. The single point energy was calculated with the TZVP-MOLOPT-GTH and TZVP-MOLOPT-SR-GTH basis set. To steer clear of the interactions between periodic images, the vacuum layers larger than 20 Å were added to non-periodic directions. The plane-waves were cut off at 400 Ry. The geometric structure figures and difference map for electron density were rendered by means of VESTA<sup>14</sup> visualization program.

The adsorption energy ( $E_{\text{ads}}$ ) was defined as:

$$E_{\text{ads}} = E_{\text{mol/surf}} - E_{\text{surf}} - E_{\text{mol(g)}}$$

where  $E_{\text{mol/surf}}$ ,  $E_{\text{surf}}$  and  $E_{\text{mol(g)}}$  are the energy of adsorbate molecule adsorbed on the surface, the energy of clean surface, and the energy of isolated molecule in a cubic periodic box, respectively.

The binding energy ( $E_{\text{bind}}$ ) was defined as:

$$E_{\text{bind}} = E_{\text{whole}} - E_{\text{BzMIM}} - E_{\text{Me-4PACz}}$$

where  $E_{\text{whole}}$ ,  $E_{\text{BzMIM}}$  and  $E_{\text{Me-4PACz}}$  are the energy of the whole system, the energy of BzMIM, and the energy of Me-4PACz, respectively.

The defect formation energy ( $E_{\text{def}}$ ) of perovskite was defined as:

$$E_{\text{def}} = E_{\text{v}} + E_{\text{pb}} - E_{\text{perf}}$$

Where  $E_{\text{v}}$ ,  $E_{\text{pb}}$  and  $E_{\text{perf}}$  are the energy of containing a surface lead vacancy, the chemical potential of a lead atom, and the energy of perfect state of the system.

## Supplementary Note 1. Cyclic Voltammetry

To characterize the surface coverage of functional materials, cyclic voltammetry (CV) experiments were conducted using a VIIUM electrochemical workstation configured with a three-electrode system at ambient temperature. The working electrodes were fabricated by spin-coating onto ITO-coated glass substrates, with an active electrode area of 0.5625 cm<sup>2</sup> (0.75 cm × 0.75 cm). A platinum plate served as the counter electrode, while an Ag/AgCl electrode (in 3.0 M KCl solution) was used as the reference electrode. Measurements were performed in an argon-purged 1,2-dichlorobenzene (o-DCB) solution containing 0.1 M tetrabutylammonium hexafluorophosphate (TBA<sup>+</sup>PF<sub>6</sub><sup>-</sup>) as the supporting electrolyte to maintain an inert and conductive medium. All potentials were calibrated against the ferrocene/ferrocenium (Fc/Fc<sup>+</sup>) redox couple as an internal reference. The effective surface coverage ( $\Gamma$ ) of ITO/NiO<sub>x</sub> Me-4PACz or ITO/NiO<sub>x</sub>/Me-4PACz/BzMIMBF<sub>4</sub> was determined by analyzing the linear relationship between the oxidative peak current and the scan rate, as detailed below:

$$I_p = \frac{n^2 F^2 A \Gamma v}{4RT}$$

Taking the scanning rate  $v$  as the horizontal axis and the current  $I_p$  as the vertical axis, we plot a scatter diagram. Thus, a linear fit on the data was performed to obtain the slope  $k$ , expressed as:

$$I_p = kv$$

According to the above formula, the surface coverage is obtained as:

$$\Gamma = \frac{4RTk}{n^2 F^2 A}$$

Where  $R$  is the gas constant ( $R=8.314 \text{ J}\cdot\text{mol}^{-1}\cdot\text{K}^{-1}$ ),  $T$  is the temperature ( $T=298 \text{ K}$ ),  $k$  is the fitting slope,  $n$  is the number of electron transfers ( $n=1$ ),  $F$  is the Faraday constant ( $F=96485 \text{ C}\cdot\text{mol}^{-1}$ ),  $A$  is the electrode area.

## Supplementary Note 2. Conductivity and hole mobility



The conductivity ( $\sigma$ ) is calculated using the following formula:

$$\sigma = \frac{d}{AR}$$

where  $R$ ,  $d$ , and  $A$  represent the resistance, thickness of HTL, and the thin film area, respectively.

The hole mobility ( $\mu$ ) was determined by analyzing the current-voltage ( $J$ - $V$ ) characteristics of the NiO<sub>x</sub>/Me-4PACz composite film using the Mott-Gurney model for trap-free semiconductors. The model is expressed as:

$$J = \frac{9\epsilon_0\epsilon_r\mu(V - V_r - V_{bi})^2}{8L^3}$$

where  $J$  is the current density,  $\epsilon_0$  is the vacuum permittivity ( $8.854 \times 10^{-12} \text{ F} \cdot \text{m}^{-1}$ ),  $\epsilon_r$  is the relative permittivity of the film,  $L$  is the film thickness,  $V$  is the applied voltage,  $V_r$  accounts for voltage losses due to contact and series resistance, and  $V_{bi}$  represents the built-in potential from the work function difference between electrodes. The hole mobility ( $\mu$ ) was extracted by fitting the  $J$ - $V$  curves to this model.

### Supplementary Note 3. Residual stress analysis by GIXRD

For GIXRD measurement, the (210) plane of perovskite featuring an XRD peak at  $31.5^\circ$  was selected is chosen as the stress-free  $2\theta$  degree due to its diversity in providing more reliable structure symmetry information, in which the  $2\theta$  is fixed while the instrument tilt angles are varied to ensure the X-ray penetration depth. The tilt angles ( $\psi$ ) are fixed at  $0^\circ$ ,  $10^\circ$ ,  $20^\circ$ ,  $30^\circ$ ,  $40^\circ$  and  $50^\circ$ , respectively. According to Bragg's Law and generalized Hooke's Law, the relationship of  $2\theta$ - $\sin^2\psi$  can be given by the following equation:

$$\sigma = -\frac{E_p}{(1 + \nu_p)} \frac{\pi}{180^\circ} \cot\theta_0 \frac{\partial(2\theta)}{\partial[(\sin\psi)^2]}$$

where  $E_p$  is the perovskite modulus (10 GPa) and  $\nu_p$  is Poisson's ratio of the perovskite (0.3)<sup>15</sup>.  $\theta_0$  is half of the scattering angle  $2\theta_0$  for stress-free perovskite ( $2\theta_0 = 31.5^\circ$ ). The residue stress of perovskite films can be calculated from equation above by fitting the  $2\theta$  as a function of  $\sin^2\psi$ , and the slope of the fitted line represents the scale of the residual strain. The negative slope indicates the films bear tensile stress, while the positive slope indicates the films bear compressive stress.

#### Supplementary Note 4. Activation energy

The activation energy can be derived using the Nernst-Einstein equation (\*):

$$\sigma(T) = \frac{\sigma_0}{T} \exp\left(-\frac{E_a}{k_B T}\right)$$

where  $k_B$  represents the Boltzmann constant,  $\sigma_0$  is a constant, and  $T$  denotes temperature.

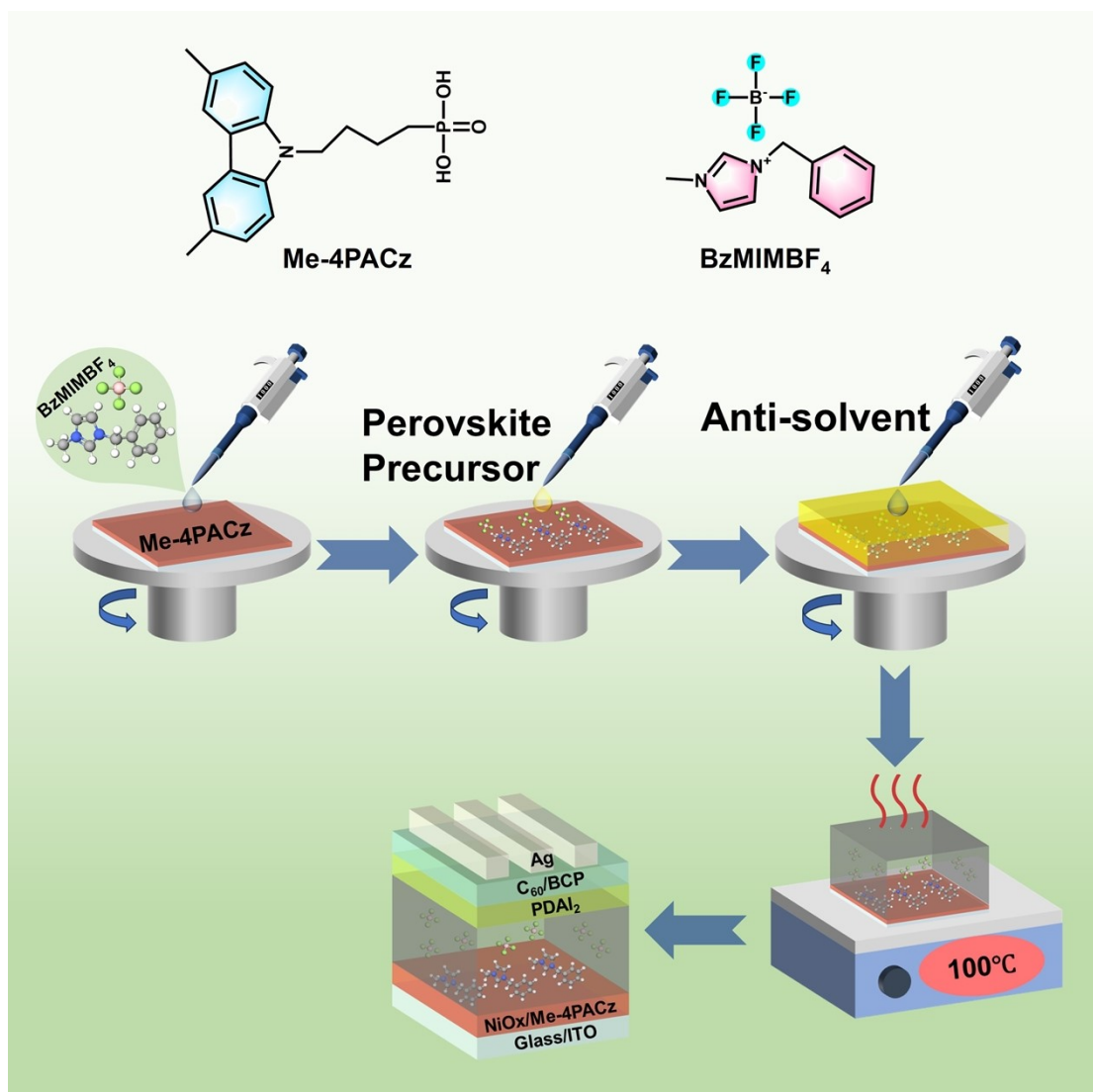


**Figure S1.** The fabrication process of BzMIMBF<sub>4</sub>-based PSC devices

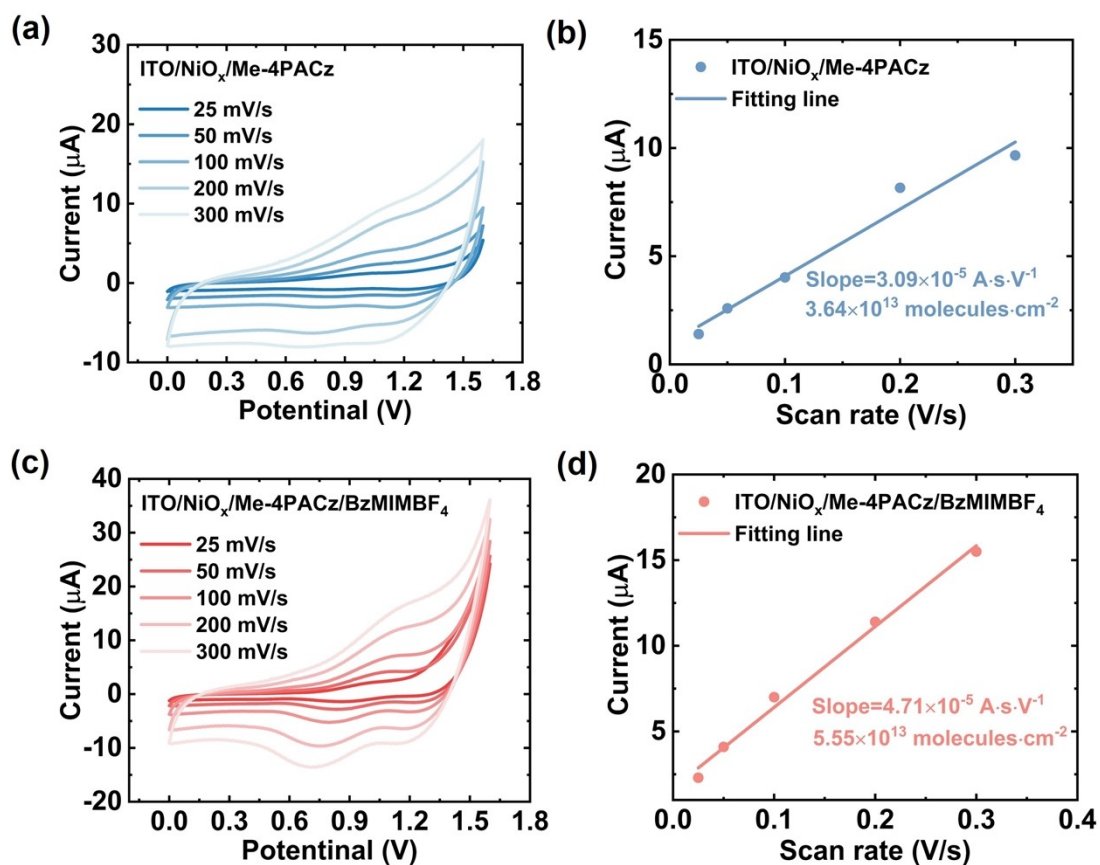


**Figure S2.** (a), (c) Cyclic voltammograms after completed electropolymerization at different scan rates for control (NiO<sub>x</sub>/Me-4PACz) and BzMIMBF<sub>4</sub>-treated (NiO<sub>x</sub>/Me-4PACz/BzMIMBF<sub>4</sub>) films. No electroactive species was added to the electrolyte solution. (b), (d) The oxidative peak current versus scan rate plots for estimation of the surface coverage from the slope of the fit.

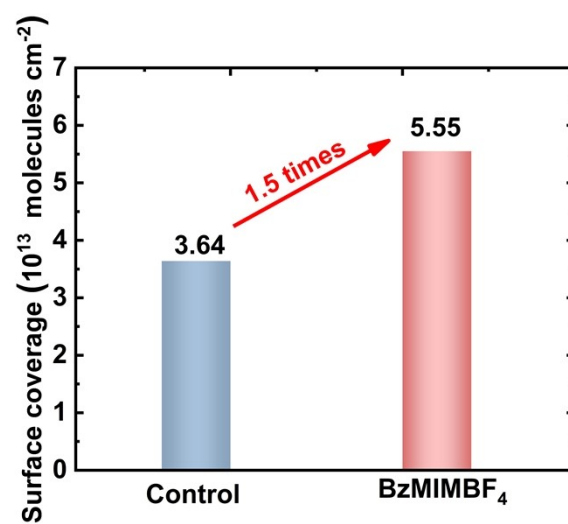


**Figure S3.** Surface coverage for the control and BzMIMBF<sub>4</sub>-treated films

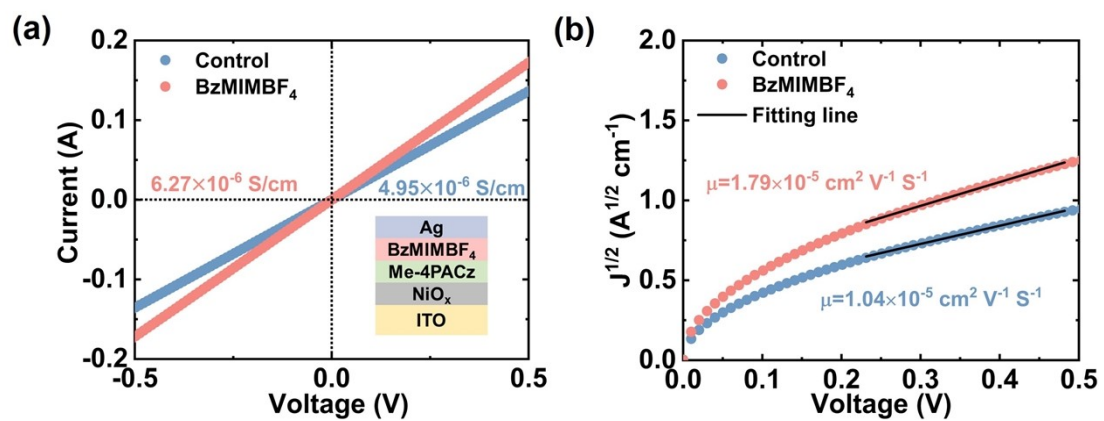


**Figure S4.** The conductivity (a) and the hole mobility (b) of control and BzMIMBF<sub>4</sub>-treated films.

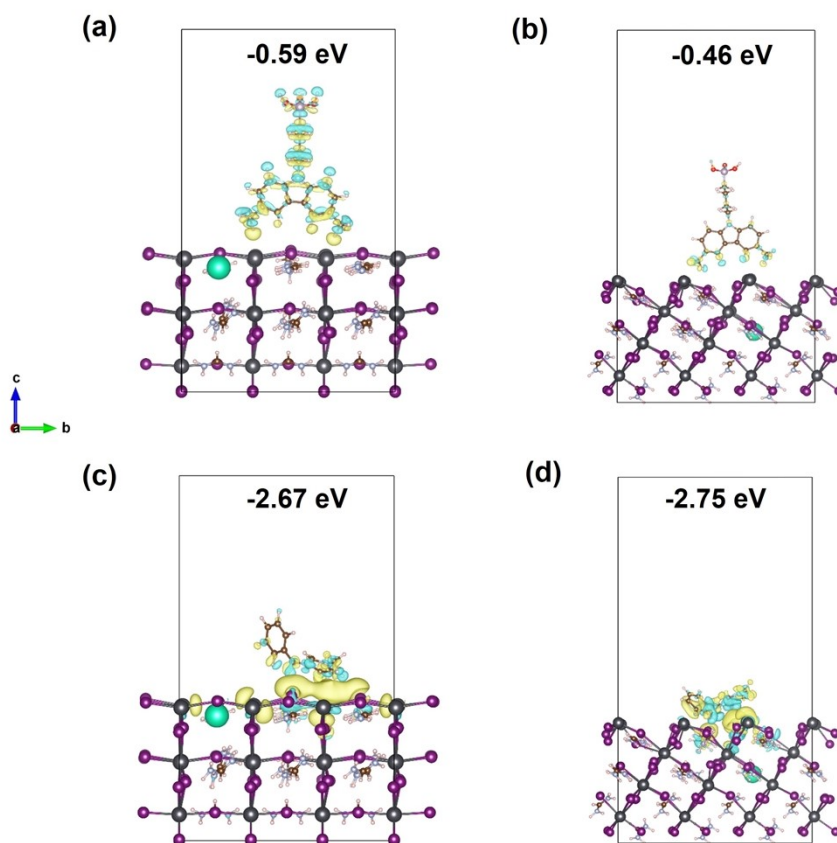


**Figure S5.** Adsorption energy of Me-4PACz on (a) (110) and (b) (111) plane. Adsorption energy of BzMIM<sup>+</sup> on (c) (110) and (d) (111) plane.

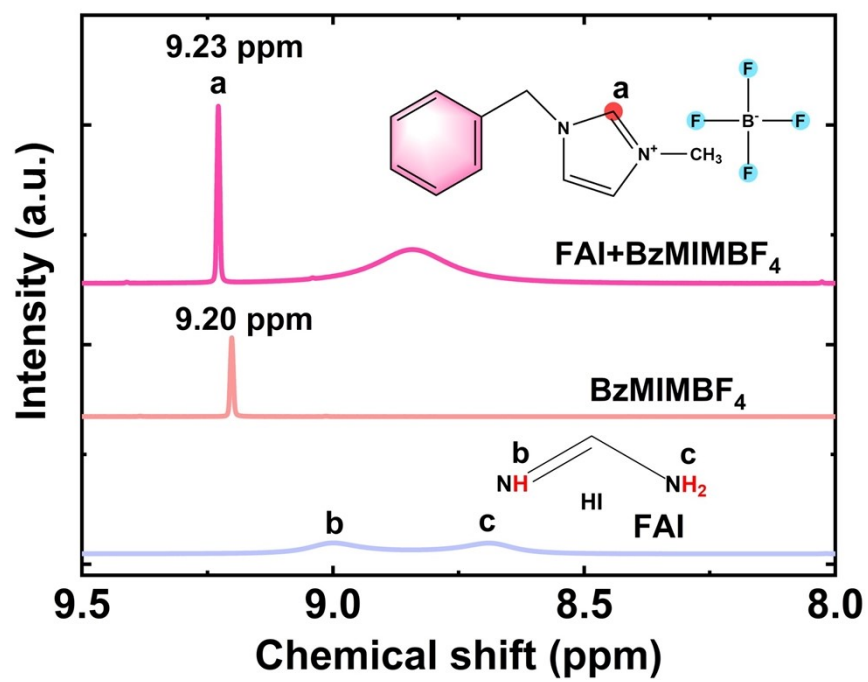


**Figure S6.**  $^1\text{H}$  NMR spectra of FAI, BzMIMBF<sub>4</sub> and BzMIMBF<sub>4</sub>/ FAI in DMSO- $\text{d}_6$ .



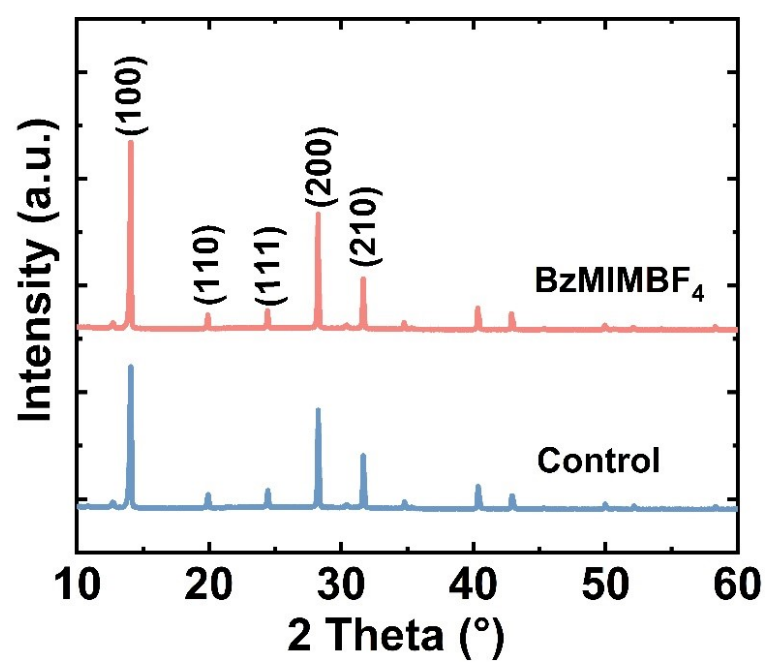


**Figure S7.** XRD patterns of control and BzMIMBF<sub>4</sub>-treated perovskite films.

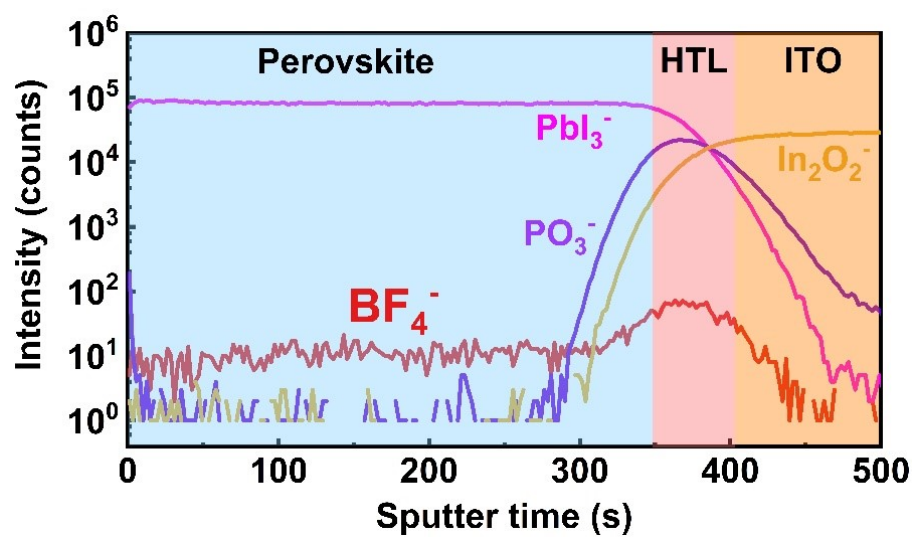
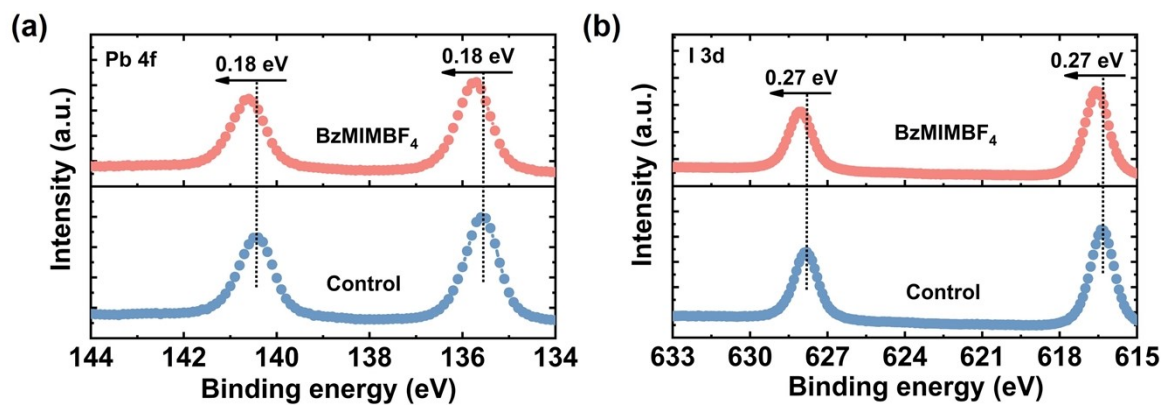
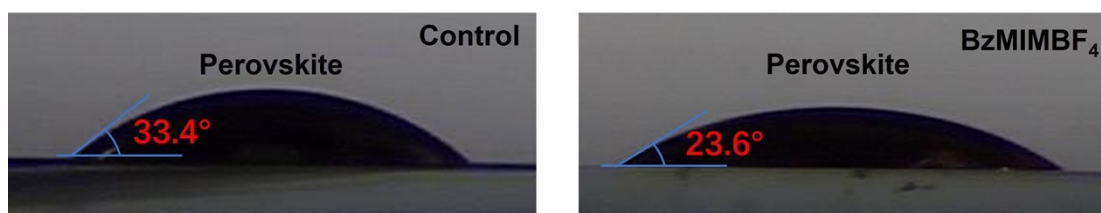


Figure S8. ToF-SIMS depth profiles of BzMIMBF<sub>4</sub>-treated perovskite films.



**Figure S9.** X-ray photoelectron spectroscopy of (a) Pb 4*f* and (b) I 3*d* for control and BzMIMBF<sub>4</sub>-treated perovskite films, respectively.



**Figure S10.** Contact angles of the perovskite precursor solution on ITO/NiO<sub>x</sub>/Me-4PACz and ITO/NiO<sub>x</sub>/Me-4PACz/BzMIMBF<sub>4</sub> surfaces.

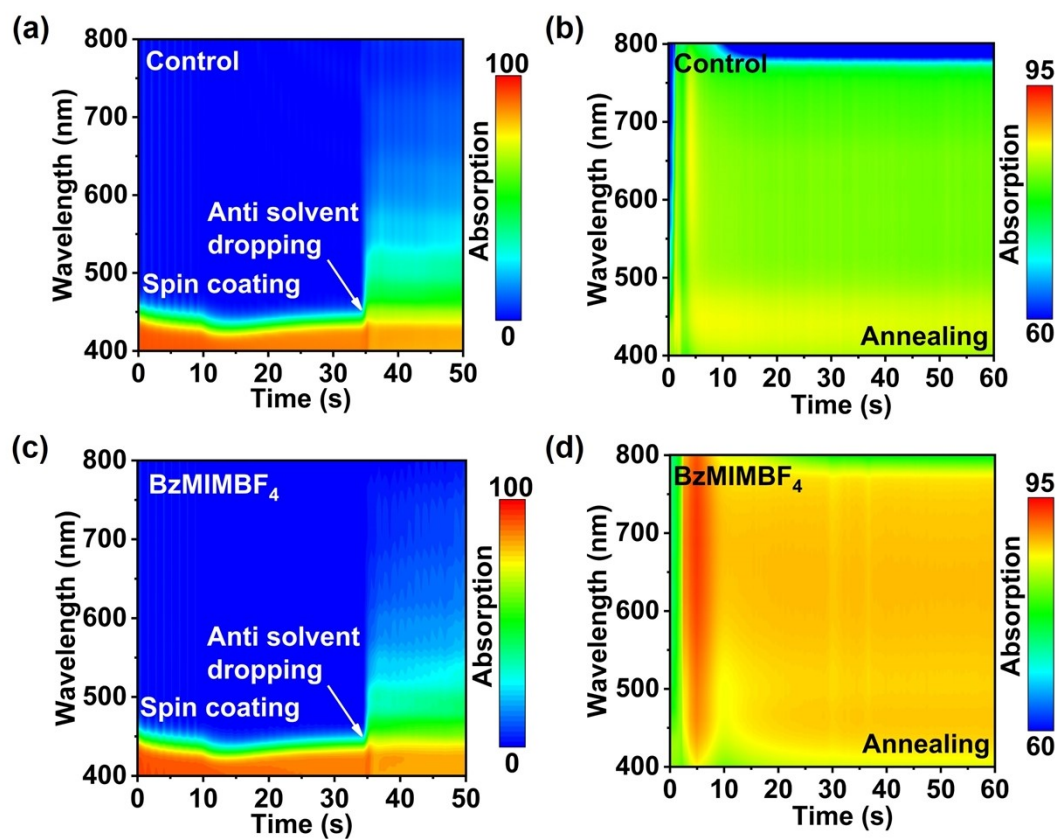


**Figure S11.** In situ absorption spectra of the control and BzMIMBF<sub>4</sub>-treated film during the spin-coating (left) and annealing (right) stages.

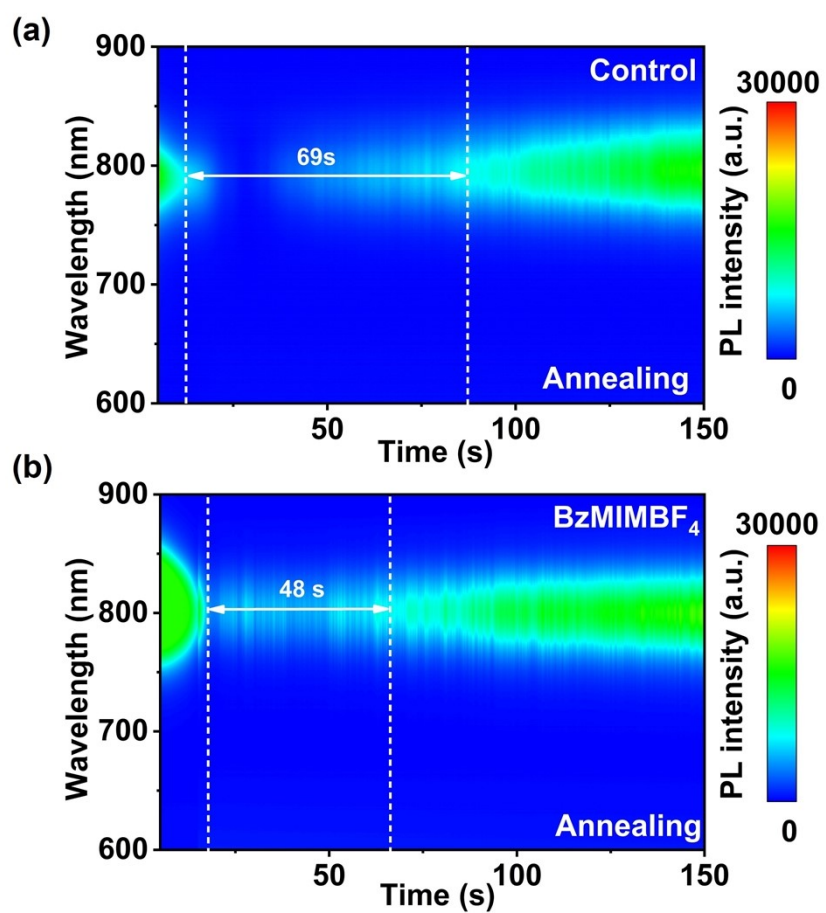


**Figure S12.** In situ PL evolution during film annealing (a detailed view of the initial 150 s).

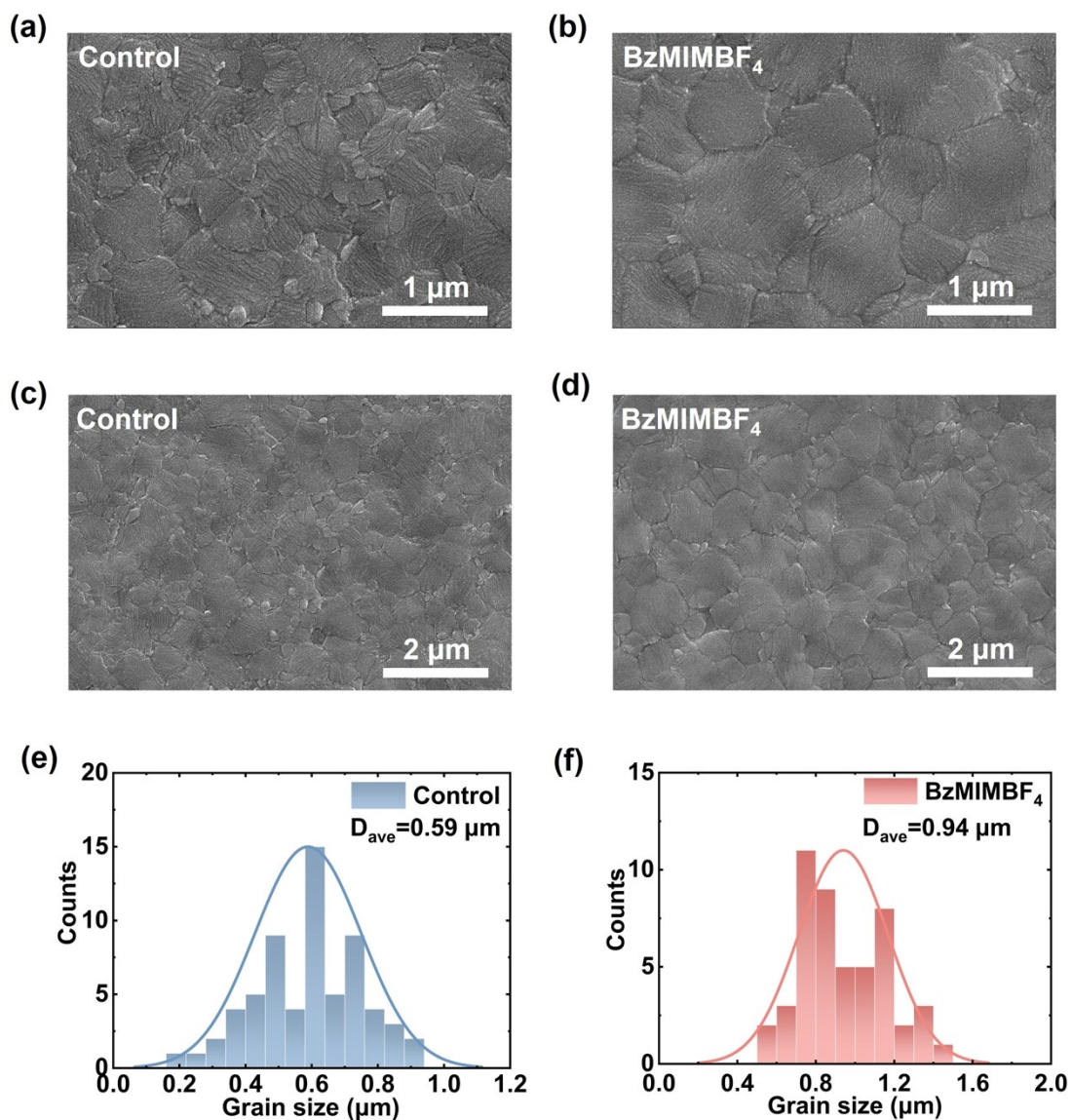


**Figure S13.** Top-view SEM images of the (a) control, (b) BzMIMBF<sub>4</sub>-treated perovskite films with a scale bar of 1  $\mu\text{m}$ . Top-view SEM images of the (c) control, (d) BzMIMBF<sub>4</sub>-treated perovskite films with a scale bar of 2  $\mu\text{m}$ . (e), (f) Grain size distribution of perovskite films, obtained from (c), (d).

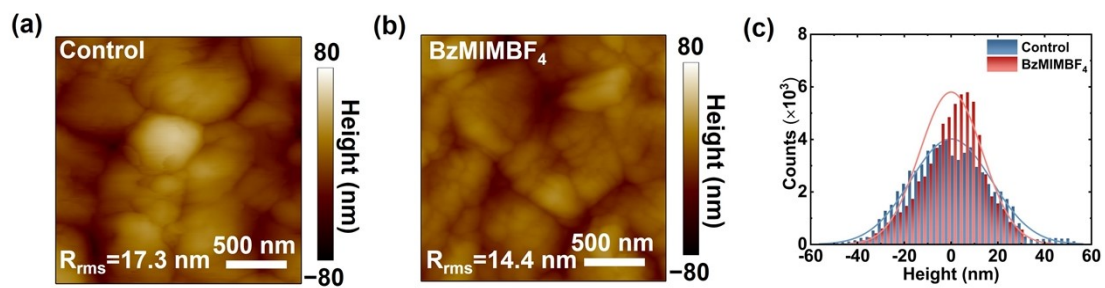


**Figure S14.** AFM images for (a) control and (b) BzMIMBF<sub>4</sub>-treated perovskite films, respectively (The testing area is 2×2 μm<sup>2</sup>). the corresponding statistical distribution of height (c) derived from AFM images.



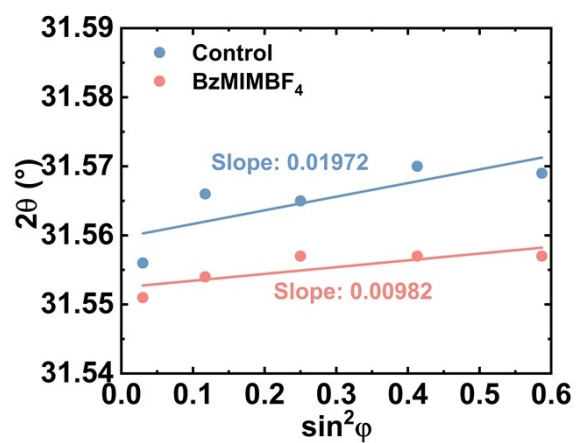


**Figure S15.** The residual strain of the corresponding diffraction peaks ( $2\theta$ ) of perovskite films based on control and BzMIMBF<sub>4</sub>-treated perovskite films as a function of  $\sin^2\psi$ .

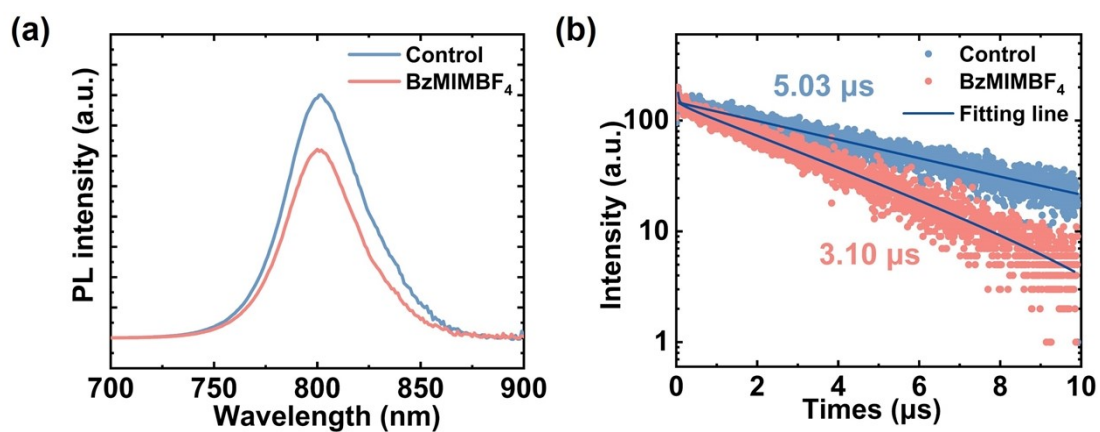


**Figure S16.** (a) Steady-state and (b) time-resolved photoluminescence (PL) spectra of perovskite films, prepared on ITO/NiO<sub>x</sub>/Me-4PACz substrates for both control and BzMIMBF<sub>4</sub>-treated samples.

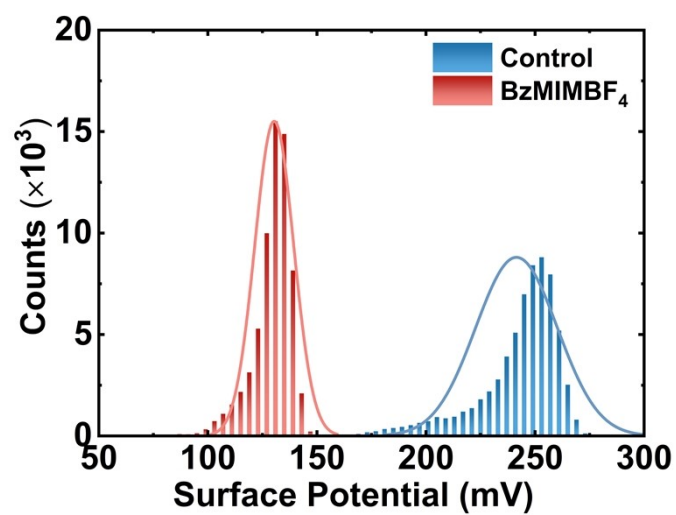


**Figure S17.** the corresponding statistical distribution of surface potential derived from KPFM images.

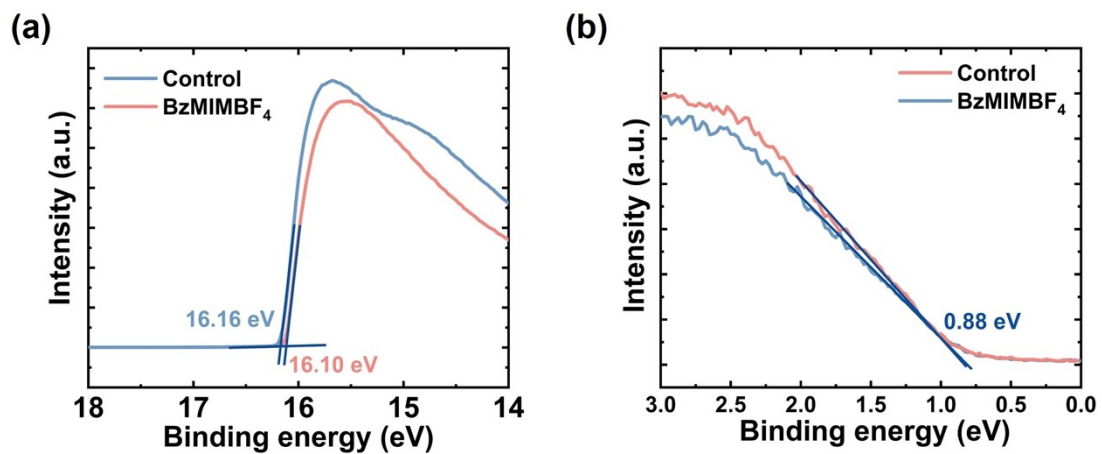


**Figure S18.** UPS energy spectra of the control and BzMIMBF<sub>4</sub>-treated perovskite films are shown in (a) (secondary electron cut-off) and (b) (valence band region). a.u. denotes arbitrary units.

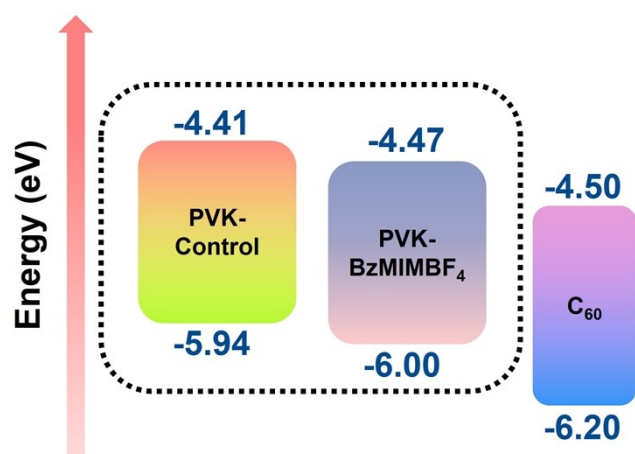


**Figure S19.** Schematic diagram of the energy level arrangement of PSCs with and without BzMIMBF<sub>4</sub>-treated perovskite films.

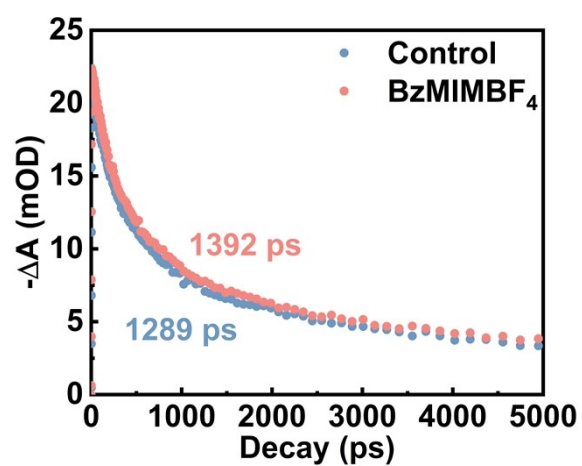


**Figure S20.** The kinetic traces for photo-bleaching probed at 810 nm of the pristine and treated perovskite film.

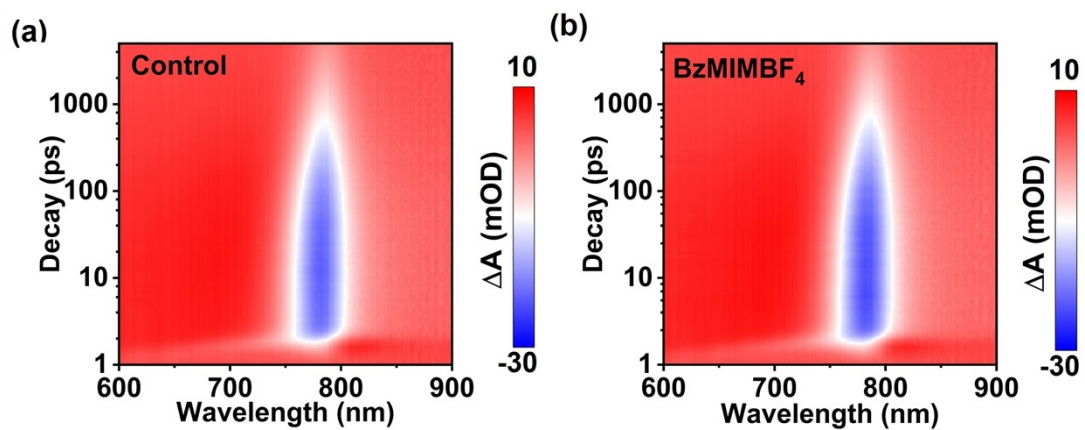


**Figure S21.** The pseudo-color TA plots of the (a) control and (b) BzMIMBF<sub>4</sub>-treated perovskite films.

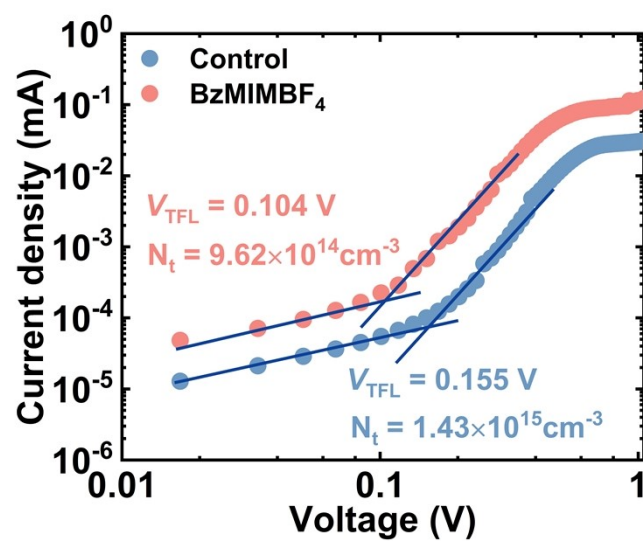


**Figure S22.** SCLC curves of hole-only devices with the structures of ITO/NiO<sub>x</sub>/Me-4PACz/perovskite/Spiro-OMeTAD.



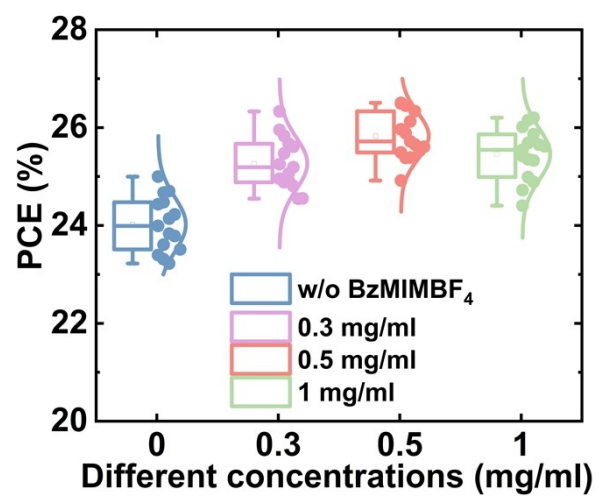


**Figure S23.** PCE statistics of PSCs with various concentrations of BMIMBF<sub>4</sub>.

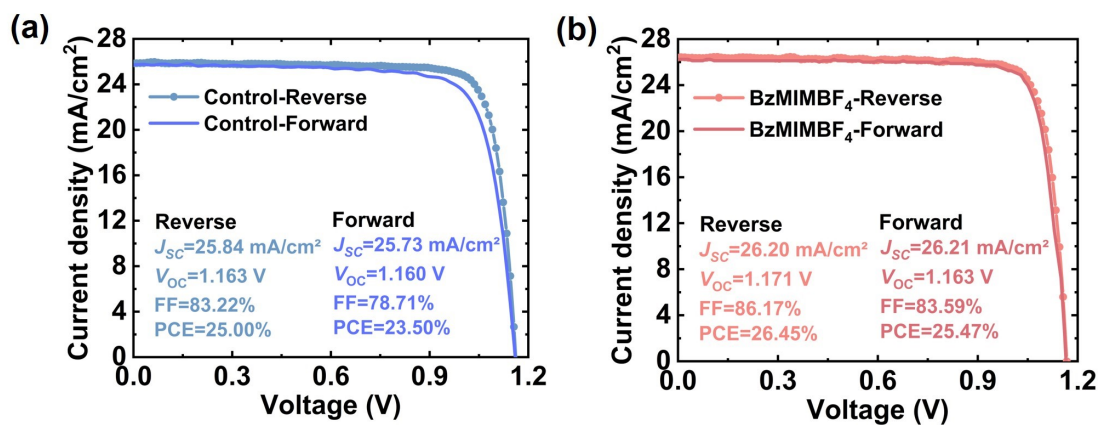


**Figure S24.** Hysteresis study of the device prepared under different conditions. a) control device, b) BMIMBF<sub>4</sub>- treated device

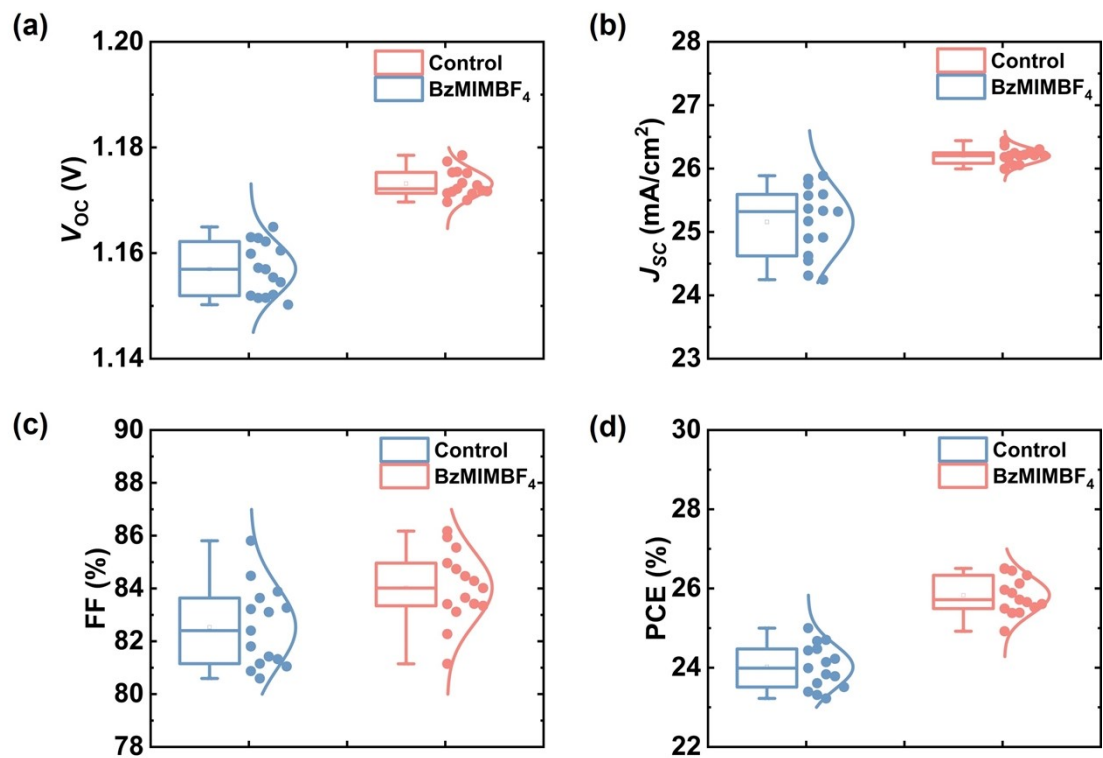


**Figure S25.** Statistical distribution of the (a)  $V_{oc}$ , (b)  $J_{sc}$ , (c) FF and (d) PCE of the PSCs prepared in different conditions. The error bars were obtained from 15 measured samples for each condition (Mask area: 0.08 cm<sup>2</sup>).

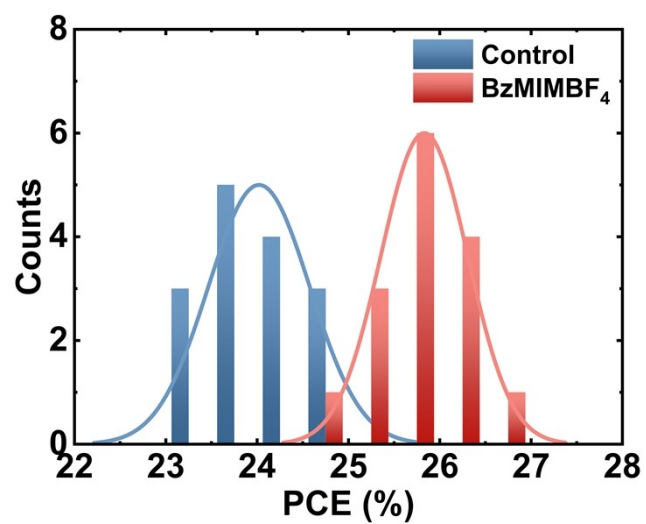


**Figure S26.** Statistics distribution of PCEs for 15 individual devices.

## 检测报告

报告编号: 检测字第 202509100013 号  
Report No.

防伪码  
5a8190813fa54ccc  
ba21edc3b8d227f0  
29249c3843b463d  
aca2ba8d4d13ac5b

样品名称: FAMACsPbI<sub>3</sub> inverted perovskite solar cells  
Sample Name  
标称生产单位: Chongqing University  
Manufacturer  
委托单位: Chongqing University  
Client  
联络信息: No. 174, Shazheng Subdistrict, Shapingba District, Chongqing, China  
Contact Information  
检测类别: Commission test  
Test Category



授权签字人: 陈清满  
Approved by

1010345583

签发日期: 2025 年 09 月 02 日  
Issue Date Year Month Day

地址: 中国·四川·成都玉观路 10 号  
Address: No. 10, Yuhuang Road, Chengdu, Sichuan, China  
邮编: 610021  
Post Code  
网址: www.nimtt.cn  
Web

电话: 028-60828828  
Telephone  
传真: 028-84404149  
Fax  
邮箱: kfzx@nimtt.com  
E-mail

第 1 页 共 5 页  
Page of

中国测试技术研究院检测报告  
Test Report of NIMTT

报告编号: 检测字第 202509100013 号  
Report No.

样品名称 Sample Name		FAMACsPbI <sub>3</sub> inverted perovskite solar cells		型号规格 Model		Single-junction perovskite solar cells	
商 标 Trade Mark		/		质量等级 Grade		/	
生产日期 Production Date		/		出厂编号/批号 Serial No. or Lot No.		CQU-LaFREMD-A10	
受检单位 Institution Inspected	名称 Name	/					
	地址 Address	/					
标称生产单位 Manufacturer		Chongqing University					
		名称 Name					
		地址 Address	No.174, Shazheng Subdistrict, Shapingba District, Chongqing, China				
委托单位 Client		Chongqing University					
		名称 Name					
		地址 Address	No.174, Shazheng Subdistrict, Shapingba District, Chongqing, China				
抽样方案 Sampling Plan		/		抽样单编号 Sampling list No.		/	
抽样人员 Sampler		/		抽样日期 Sampling Date		/	
抽样地点 Sampling Site		/		抽样数量 Sampling Quantity		/	
抽样基数 Basic Number for Sampling		/		到样日期 Receipt Date		2025 年 09 月 01 日	
送样数量 Sample Quantity		1		样品状态 Sample Status		Intact	
检测地点 Test Location		No.10 Yushuang Road, Chengdu, Sichuan Province, China			检测日期 Test Date		2025 年 09 月 01 日
检测依据 Test Method		IEC 60904-1:2020 光伏器件 第 1 部分:光伏电流-电压特性的测量					

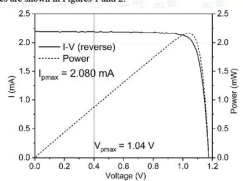
续页专用 (v202001)  
Continued Page

第 3 页 共 5 页  
Page of

中国测试技术研究院检测报告  
Test Report of NIMTT

报告编号: 检测字第 202509100013 号  
Report No.

## 检测结果

<p><b>1. Test Condition</b> Reference Cell: Mono-Si solar cell (window material: KG1). Sample Information: FAMACsPbI<sub>3</sub> inverted perovskite solar cells. Dimensions: (1.5×1.5) cm<sup>2</sup>. Aperture area: 0.082 cm<sup>2</sup>. Storage Condition of Sample Before Test: Temperature: 25±5°C; N<sub>2</sub> atmosphere; stored in dark for 3 Days.</p> <p><b>2. Methodologies and Settings</b> (1) In the 3A steady-state solar simulator (spectrum: AM1.5), the irradiance of the solar simulator was first calibrated to 1000 W/m<sup>2</sup> with a standard solar cell, the temperature of the solar cell was controlled by a water bath thermostat at 25°C, and then the I-V parameters of the tested sample were measured with a digital source meter. (2) The parameter settings of the measurement software are shown in Table 1:</p> <p>Table 1 Parameter Settings for I-V Test</p> <table> <tr> <th>Scan Mode</th><th>Start Voltage(V)</th><th>End Voltage(V)</th><th>Step (V)</th><th>Sweep point delay(ms)</th><th>Number of point</th><th>Light Soaking Pre-treatment</th></tr> <tr> <td>Reverse scan</td><td>1.3</td><td>-0.1</td><td>0.01</td><td>40</td><td>140</td><td>YES</td></tr> <tr> <td>Forward scan</td><td>-0.1</td><td>1.3</td><td>0.01</td><td>40</td><td>140</td><td>YES</td></tr> </table>							Scan Mode	Start Voltage(V)	End Voltage(V)	Step (V)	Sweep point delay(ms)	Number of point	Light Soaking Pre-treatment	Reverse scan	1.3	-0.1	0.01	40	140	YES	Forward scan	-0.1	1.3	0.01	40	140	YES
Scan Mode	Start Voltage(V)	End Voltage(V)	Step (V)	Sweep point delay(ms)	Number of point	Light Soaking Pre-treatment																					
Reverse scan	1.3	-0.1	0.01	40	140	YES																					
Forward scan	-0.1	1.3	0.01	40	140	YES																					
<p><b>3. Test Results</b> Current-voltage (I-V) curves are shown in Figures 1 and 2:</p>  <p>Figure 1 I-V Curve (Reverse Scan)</p>																											

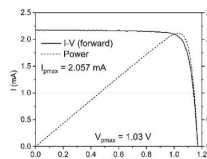
续页专用 (v202001)  
Continued Page

第 4 页 共 5 页  
Page of

中国测试技术研究院检测报告  
Test Report of NIMTT

报告编号: 检测字第 202509100013 号  
Report No.

## 检测结果

 <p>Figure 2 I-V Curve (Forward Scan)</p>																															
<p>Table 2 Irradiated I-V parameters</p> <table> <tr> <th>Scan Mode</th><th>Short-circuit Current I<sub>sc</sub> (mA)</th><th>Open-circuit Voltage V<sub>oc</sub> (V)</th><th>Fill Factor FF (%)</th><th>Maximum Power P<sub>max</sub> (mW)</th><th>Maximum Power Voltage V<sub>mp</sub> (V)</th><th>Maximum Power Current I<sub>mp</sub> (mA)</th><th>Conversion Efficiency η (%)</th></tr> <tr> <td>Reverse scan</td><td>2.185</td><td>1.174</td><td>84.28</td><td>2.162</td><td>1.04</td><td>2.080</td><td>26.37</td></tr> <tr> <td>Forward scan</td><td>2.173</td><td>1.171</td><td>83.30</td><td>2.119</td><td>1.03</td><td>2.057</td><td>25.84</td></tr> </table>								Scan Mode	Short-circuit Current I <sub>sc</sub> (mA)	Open-circuit Voltage V <sub>oc</sub> (V)	Fill Factor FF (%)	Maximum Power P <sub>max</sub> (mW)	Maximum Power Voltage V <sub>mp</sub> (V)	Maximum Power Current I <sub>mp</sub> (mA)	Conversion Efficiency η (%)	Reverse scan	2.185	1.174	84.28	2.162	1.04	2.080	26.37	Forward scan	2.173	1.171	83.30	2.119	1.03	2.057	25.84
Scan Mode	Short-circuit Current I <sub>sc</sub> (mA)	Open-circuit Voltage V <sub>oc</sub> (V)	Fill Factor FF (%)	Maximum Power P <sub>max</sub> (mW)	Maximum Power Voltage V <sub>mp</sub> (V)	Maximum Power Current I <sub>mp</sub> (mA)	Conversion Efficiency η (%)																								
Reverse scan	2.185	1.174	84.28	2.162	1.04	2.080	26.37																								
Forward scan	2.173	1.171	83.30	2.119	1.03	2.057	25.84																								
备注 Note	<p>1. Reported performance parameters take the average of three test values. 2. The solar cell area data is determined according to the mask area.</p>																														

审核人员: 吴伟钢  
Verified by

主检人员: 陈永李  
Tested by

续页专用 (v202101)  
Continued Page

第 5 页 共 5 页  
Page of

**Figure S27.** Certified PCE of BMIMBF<sub>4</sub>-treated device, as verified by the National Institute of Measurement and Testing Technology (China).

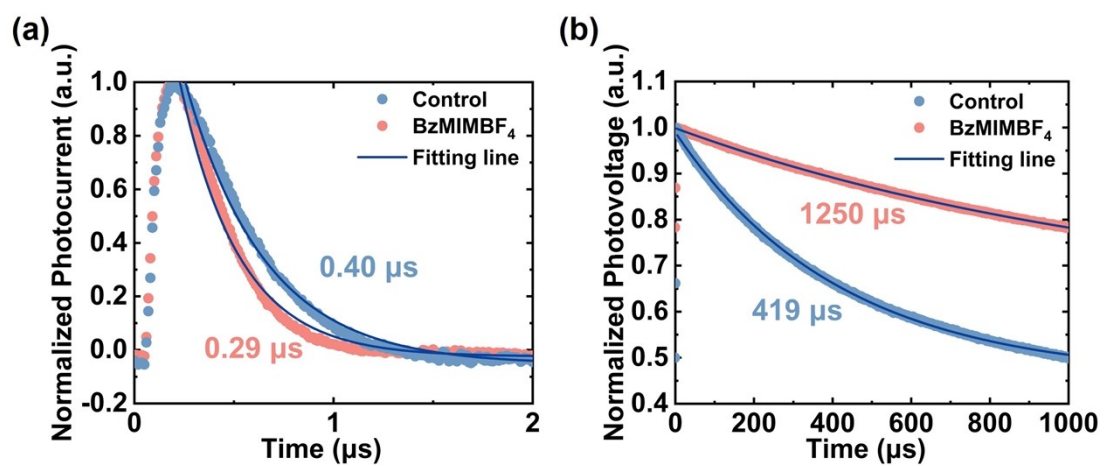


**Figure S28.** Transient photocurrent (TPC) decay and Transient photovoltage (TPV) decay for control and BMIMBF<sub>4</sub>-treated devices.

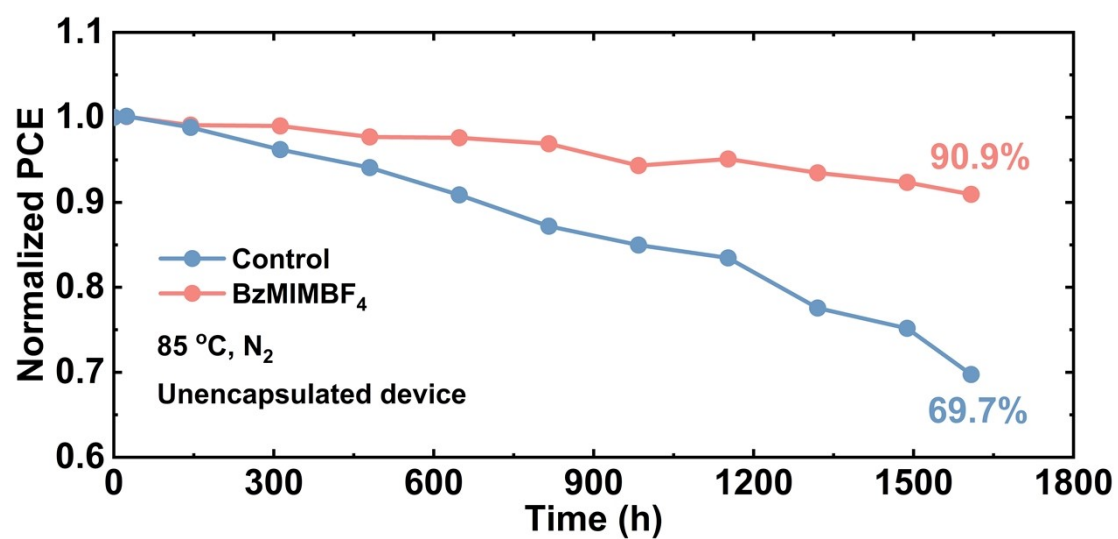


**Figure S29.** Long-term thermal stability of the unencapsulated device. Normalized PCE retention over time during aging at 85 °C in a dark N<sub>2</sub> environment.

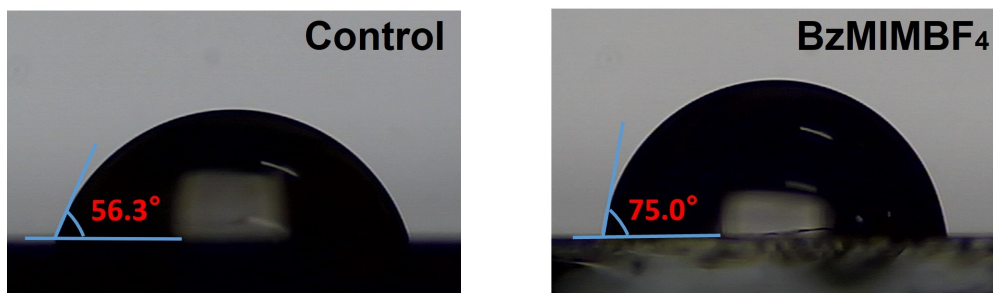


**Figure S30.** Water Contact angle measurements on the surface of perovskite films.



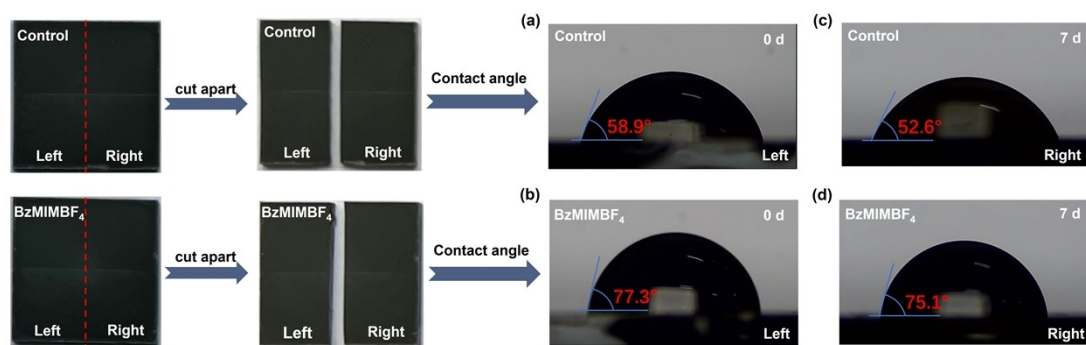


**Figure S31.** Water contact angle measurements demonstrating the long-term surface hydrophobicity of perovskite films. Freshly prepared films were immediately cut into two halves. The “left” half was measured on day 0, while the “right” half was stored in the dark at 20 °C and 20% RH for 7 days prior to measurement. (a), (c) Control films without BzMIMBF<sub>4</sub> treatment: 58.9° (day 1) → 52.6° (day 7). (b), (d) BzMIMBF<sub>4</sub>-treated films: 77.3° (day 1) → 75.1° (day 7).

**Table S1.** Fitted results of TRPL curves of the perovskite films deposited on ITO/NiO<sub>x</sub>/Me-4PACz from perovskite side.

Samples	$\tau_1$ ( $\mu$ s)	$A_1$	$\tau_2$ ( $\mu$ s)	$A_2$	$\tau_{\text{ave}}$ ( $\mu$ s)
Control	0.02	0.22	5.07	0.15	5.03
BzMIMBF <sub>4</sub>	0.26	0.01	3.12	0.14	3.10

**Table S2.** Performance summary of state-of-art p-i-n PSCs with perovskite/HTL buried interface treatment.

Source	Perovskite solar cells structure	PCE (%)	Certified PCE (%)	Year [Ref.]
<i>Adv. Mater.</i>	ITO/MeO-2PACz/ <b>CB-PA</b> /Perovskite/PCBM/BCP/Ag	25.27	/	2025[15]
<i>Adv. Funct. Mater.</i>	ITO/Me-4PACz/ <b>FBA</b> /Perovskite/C <sub>60</sub> /BCP/Ag	25.58	/	2025[16]
<i>Adv. Mater.</i>	ITO/2PACz- <b>BMIMTFSI</b> /Perovskite/LiF/C <sub>60</sub> /BCP/Ag	25.68	/	2025[17]
<i>Energy Environ. Sci.</i>	FTO/NiO <sub>x</sub> /MeO-2PACz/ <b>TFSA</b> /Perovskite/C <sub>60</sub> /BCP/Ag	25.92	25.77	2024[18]
<i>Adv. Funct. Mater.</i>	FTO/2PACz+Me-4PACz/ <b>BFS</b> /Perovskite/3MPTAI/C <sub>60</sub> /BCP/Ag	26.16	/	2025[19]
<i>Adv. Mater.</i>	ITO/NiO <sub>x</sub> /Me-4PACz- <b>PM</b> /Perovskite/C <sub>60</sub> /BCP/Ag	26.34	25.48	2025[20]
<i>Nat. Chem.</i>	FTO/NiO <sub>x</sub> /Me-4PACz/ <b>2DPAA</b> /Perovskite/C <sub>60</sub> /BCP/Ag	26.53	26.02	2025[21]
<i>Nature</i>	ITO/NiO/ <b>NA</b> -Me-4PACz/Perovskite/PI/PCBM/BCP/Ag	26.54	/	2024[22]
<i>Adv. Mater.</i>	ITO/NiO <sub>x</sub> /Me-4PACz/ <b>4Br-BPA</b> /Perovskite/C <sub>60</sub> /BCP/Ag	26.59	26.12	2025[23]
<i>Energy Environ. Sci.</i>	FTO/MeO-4PACz/Al <sub>2</sub> O <sub>3</sub> - <b>2-ATCI</b> /Perovskite/PCBM/BCP/Ag	26.63	26.42	2025[24]
<i>Adv. Mater.</i>	FTO/NiO <sub>x</sub> /Me-4PACz/ <b>AG</b> /Perovskite/C <sub>60</sub> /BCP/Ag	26.74	26.21	2025[25]
<b>This work</b>	ITO/NiO <sub>x</sub> /Me-4PACz/ <b>BzMIMBF<sub>4</sub></b> /Perovskite/C <sub>60</sub> /BCP/Ag	<b>26.45</b>	<b>26.37</b>	/

## References:

- 1 M. J. Frisch, G. W. Trucks, H. B. Schlegel, G. E. Scuseria, M. A. Robb, J. R. Cheeseman, G. Scalmani, V. Barone, G. A. Petersson, H. Nakatsuji, X. Li, M. Caricato, A. V. Marenich, J. Bloino, B. G. Janesko, R. Gomperts, B. Mennucci, H. P. Hratchian, J. V. Ortiz, A. F. Izmaylov, J. L. Sonnenberg, Williams, F. Ding, F. Lipparini, F. Egidi, J. Goings, B. Peng, A. Petrone, T. Henderson, D. Ranasinghe, V. G. Zakrzewski, J. Gao, N. Rega, G. Zheng, W. Liang, M. Hada, M. Ehara, K. Toyota, R. Fukuda, J. Hasegawa, M. Ishida, T. Nakajima, Y. Honda, O. Kitao, H. Nakai, T. Vreven, K. Throssell, J. A. Montgomery Jr., J. E. Peralta, F. Ogliaro, M. J. Bearpark, J. J. Heyd, E. N. Brothers, K. N. Kudin, V. N. Staroverov, T. A. Keith, R. Kobayashi, J. Normand, K. Raghavachari, A. P. Rendell, J. C. Burant, S. S. Iyengar, J. Tomasi, M. Cossi, J. M. Millam, M. Klene, C. Adamo, R. Cammi, J. W. Ochterski, R. L. Martin, K. Morokuma, O. Farkas, J. B. Foresman and D. J. Fox, *Journal*, 2016.
- 2 P. J. Stephens, F. J. Devlin, C. F. Chabalowski and M. J. Frisch, *J. Phys. Chem.*, 1994, **98**, 11623-11627.
- 3 S. Grimme, S. Ehrlich and L. Goerigk, *J. Comput. Chem.*, 2011, **32**, 1456-1465.
- 4 S. Grimme, J. Antony, S. Ehrlich and H. Krieg, *J. Chem. Phys.*, 2010, **132**.
- 5 F. Weigend and R. Ahlrichs, *Phys. Chem. Chem. Phys.*, 2005, **7**, 3297-3305.
- 6 D. Rappoport and F. Furche, *J. Chem. Phys.*, 2010, **133**.
- 7 T. Lu and Q. Chen, *Chemistry - Methods*, 2021, **1**, 231-239.
- 8 T. Lu and F. Chen, *J. Comput. Chem.*, 2012, **33**, 580-592.
- 9 T. Lu, *J. Chem. Phys.*, 2024, **161**.
- 10 T. Lu, *J. Chem. Phys.*, 2024, **161**.
- 11 W. Humphrey, A. Dalke and K. Schulten, *J. Mol. Graph.*, 1996, **14**, 33-38.
- 12 T. D. Kühne, M. Iannuzzi, M. Del Ben, V. V. Rybkin, P. Seewald, F. Stein, T. Laino, R. Z. Khaliullin, O. Schütt, F. Schiffmann, D. Golze, J. Wilhelm, S. Chulkov, M. H. Bani-Hashemian, V. Weber, U. Borštnik, M. Taillefumier, A. S. Jakobovits, A. Lazzaro, H. Pabst, T. Müller, R. Schade, M. Guidon, S. Andermatt, N. Holmberg, G. K. Schenter, A. Hehn, A. Bussy, F. Belleflamme, G. Tabacchi, A. Glöb, M. Lass, I. Bethune, C. J. Mundy, C. Plessl, M. Watkins, J. VandeVondele, M. Krack and J. Hutter, *J. Chem. Phys.*, 2020, **152**, 194103.
- 13 J. VandeVondele and J. Hutter, *J. Chem. Phys.*, 2007, **127**, 114105.
- 14 K. Momma and F. Izumi, *J. Appl. Crystallogr.*, 2011, **44**, 1272-1276.
- 15 B. Yu, K. Wang, Y. Sun and H. Yu, *Adv. Mater.*, 2025, **37**, e2500708.
- 16 F. Yuan, T. Xue, M. Du, H. Huang, R. Zeng, L. Li, C. Wang, Z. Song, Q. Guo, X. Hu and E. Zhou, *Adv. Funct. Mater.*, 2025, **35**, 2425145.
- 17 Z. Feng, X. Liu, T. Tian, Z. Zhu, R. Jiang, J. Li, Y. Yuan, J. Gong, G. Gao, J. Tong, Y. Peng, S. Bai, F. Huang, X. Xiao, P. Muller-Buschbaum, Y. B. Cheng and T. Bu, *Adv. Mater.*, 2025, **37**, e2412692.
- 18 X. Chen, Q. Wang, H. Wei, J. Yang, Y. Yao, W. Tang, W. Qiu, X. Xu, L. Song, Y. Wu and Q. Peng, *Energy Environ. Sci.*, 2024, **17**, 7342-7354.

- 19 C. Li, L. Zha, H. Liu, H. Zhang, W. Ding, Y. Gao, Y. Chen, X. Lu, C. Duan, S. Liu and G. Cai, *Adv. Funct. Mater.*, 2025, e20372.
- 20 W. Yang, Y. Lin, W. Zhu, F. Du, J. Liu, Y. Ren, H. Wang, J. Liao, D. Yu, G. Fang, M. Li, R. Zhang, S. Yang and C. Liang, *Adv. Mater.*, 2025, **37**, e2502865.
- 21 Y. Peng, Y. Chen, J. Zhou, C. Luo, W. Tang, Y. Duan, Y. Wu and Q. Peng, *Nat. Commun.*, 2025, **16**, 1252.
- 22 S. Liu, J. Li, W. Xiao, R. Chen, Z. Sun, Y. Zhang, X. Lei, S. Hu, M. Kober-Czerny, J. Wang, F. Ren, Q. Zhou, H. Raza, Y. Gao, Y. Ji, S. Li, H. Li, L. Qiu, W. Huang, Y. Zhao, B. Xu, Z. Liu, H. J. Snaith, N. G. Park and W. Chen, *Nature*, 2024, **632**, 536-542.
- 23 M. Gao, Z. Ou, C. Wang, L. Liu, D. Hu, W. Wan, P. Chen, Y. Pan, S. Nie, Y. Luo, P. Zhang, D. Peng, K. Zhao, M. Fu, W. Liu, X. Wang, W. Zhang, H. Guo, Y. Zheng, Z. Xiao, X. Gao, Z. Ma, R. Wang, T. Jiang and K. Sun, *Adv. Mater.*, 2025, e14273.
- 24 Q. Li, M. Wang and L. Li, *Energy Environ. Sci.*, 2025, **18**, 10228-10237.
- 25 M. Cheng, Y. Duan, D. Zhang, Z. Xie, H. Li, Q. Cao, Z. Qiu, Y. Chen and Q. Peng, *Adv. Mater.*, 2025, **37**, e2419413.